



Excitons bound by photon exchange

Erika Cortese^{1,5}, Ngoc-Linh Tran^{2,5}, Jean-Michel Manceau², Adel Bousseksou², Iacopo Carusotto³,
Giorgio Biasiol⁴, Raffaele Colombelli²✉ and Simone De Liberato¹✉

In contrast to interband excitons in undoped quantum wells, doped quantum wells do not display sharp resonances due to excitonic bound states. The effective Coulomb interaction between electrons and holes in these systems typically leads to only a depolarization shift of the single-electron intersubband transitions¹. Non-perturbative light-matter interaction in solid-state devices has been investigated as a pathway to tuning optoelectronic properties of materials^{2,3}. A recent theoretical work⁴ predicted that when the doped quantum wells are embedded in a photonic cavity, emission-reabsorption processes of cavity photons can generate an effective attractive interaction that binds electrons and holes together, leading to the creation of an intraband bound exciton. Here, we spectroscopically observe such a bound state as a discrete resonance that appears below the ionization threshold only when the coupling between light and matter is increased above a critical value. Our result demonstrates that two charged particles can be bound by the exchange of transverse photons. Light-matter coupling can thus be used as a tool in quantum material engineering, tuning electronic properties of semiconductor heterostructures beyond those permitted by mere crystal structures, with direct applications to mid-infrared optoelectronics.

Improvements in resonator design and fabrication have allowed investigation of the strong light-matter coupling regime in a multitude of solid-state devices⁵. In such a regime, the excitations of the system are not photons or matter resonances, but polaritons, hybrid quasiparticles that are linear superpositions of the two.

If the light-matter coupling is strong enough to couple multiple matter resonances, characterized by different spatial wavefunctions, to the same photonic mode, the ensuing polariton wavefunction will be a linear superposition of the uncoupled ones that possesses its own unique features, a priori different from those of the uncoupled modes. Such a phenomenon, referred to as very strong coupling^{6–8}, has only recently been experimentally demonstrated in inorganic microcavities, where it can be observed as a change in the exciton radius^{9,10}.

The question of whether such a mechanism can be pushed to the extreme, non-perturbatively modifying the excitation wavefunction and creating localized bound states from delocalized ones, has recently been theoretically investigated, leading to the prediction of discrete resonances below the continuum ionization threshold for large enough values of the light-matter coupling strengths⁴. The lower edge of the continuum corresponds to free electrons with no kinetic energy. Discrete resonances below the ionization threshold generated by the coupling with the photonic resonator must therefore be bound, as electrons do not have enough energy to escape to infinity.

The system investigated in an earlier study⁴ (a set of microcavities embedded in n-doped semiconductor quantum wells (QWs)) is particularly suitable to highlight this physics. First, it allows large light-matter coupling strengths to be achieved^{11,12} that can be tuned by changing the electronic density in the QWs¹³. Second, it is possible to design QWs narrow enough to have a single localized electronic subband, and as such no bound-to-bound intersubband transitions. Third, in such a system the Coulomb interaction does not create bound states. The two last points imply that the bare QWs with no surrounding photonic resonator do not present any discrete resonance at all, only a continuum absorption band at frequencies larger than the ionization threshold. Initially demonstrated in ref. ¹, the absence of Coulomb-bound intersubband states stems from the quasiparallel dispersion of the two electronic subbands, which leads to a repulsive electron-hole interaction.

This is in stark contrast to the case of interband transitions at shorter wavelengths, where the electron-hole interaction is attractive and leads to the creation of narrow resonances out of the electron-hole continuum in the absence of polaritonic effects: excitons in undoped samples¹⁴ and Mahan singularities in doped ones¹⁵. Polariton formation can thus modify the existing resonances as shown in ref. ¹⁰, but doesn't lead to the creation of new localized electronic resonances.

In Fig. 1, we present a sketch of this phenomenon, useful for understanding where the analogy with the most widely studied case of interband transitions in undoped QWs breaks down. In the case of interband transitions in undoped QWs, the electrons participating in the transition initially occupy the valence band, which has a negative effective mass. In the case of intersubband transitions in doped QWs, however, the same role is played by the first, partially filled conduction subband, which has a positive effective mass. Under the usual electron-hole mapping¹⁶, this leads to a positively charged hole with a negative effective mass. The effective electron mass in the excited subband m_2 in GaAs QWs is larger than the mass in the first subband m_1 (ref. ¹). This leads to a negative reduced mass of the intersubband electron-hole pair $m_r^{-1} = m_2^{-1} - m_1^{-1}$. In the presence of any attractive two-body potential, a negative reduced mass results in a repulsive electron-hole interaction, which in turn cannot create bound states. This can be intuitively understood by observing that the classical equation of motion for the electron-hole pair is symmetric under sign exchange of both hole charge and reduced mass.

Note that this argument considers only the two-body interactions between electrons and holes. Interactions mediated by bosonic fields can, and do, create attractive interactions between particles of the same charge. This is the case for the light-matter interaction considered here, and most famously demonstrated in a many-body context by the phenomenon of Cooper pairing¹⁷.

¹School of Physics and Astronomy, University of Southampton, Southampton, UK. ²Centre de Nanosciences et de Nanotechnologies (C2N), CNRS UMR 9001, Université Paris-Saclay, Palaiseau, France. ³INO-CNR BEC Center and Dipartimento di Fisica, Università di Trento, Povo, Italy. ⁴Laboratorio TASC, CNR-IOM, Trieste, Italy. ⁵These authors contributed equally to this work. Erika Cortese, Ngoc-Linh Tran. ✉e-mail: raffaele.colombelli@u-psud.fr; s.de-liberato@soton.ac.uk

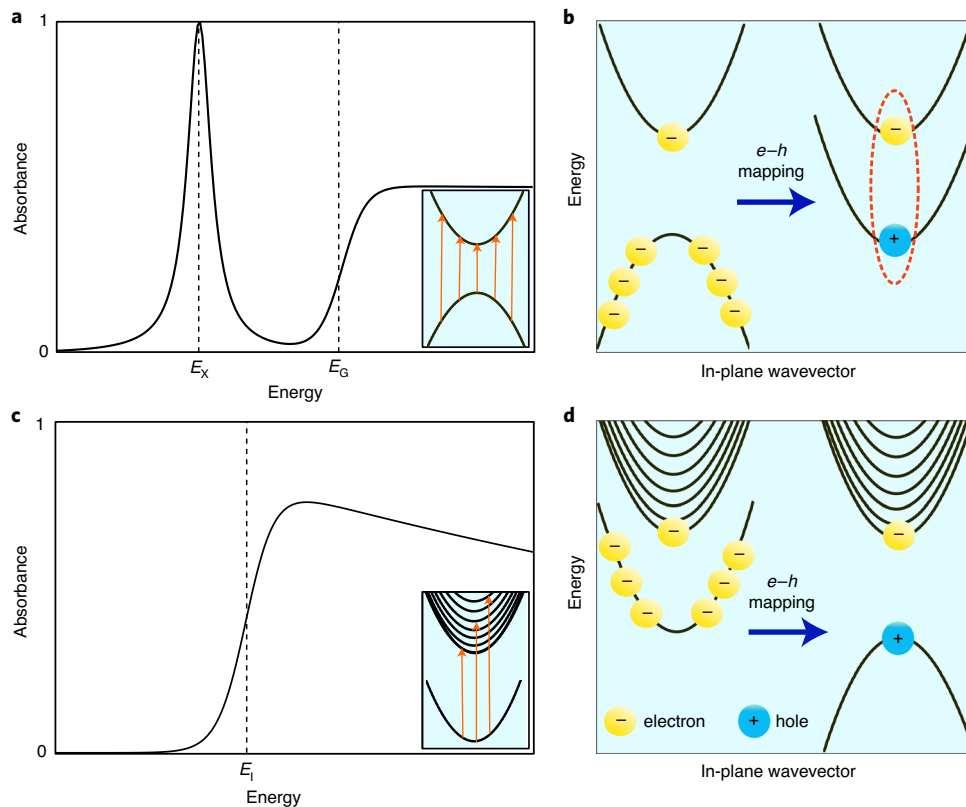


Fig. 1 | Coulomb effect in doped and undoped quantum wells. **a**, Interband absorbance of an undoped semiconductor QW, dominated by an excitonic resonance (E_x) below the bandgap energy (E_g) and the electron-hole continuum above it. Inset, illustration of the origin of the continuum part of the spectrum, understandable in a single-electron picture as interband transitions of electrons with different in-plane wavevectors. **b**, Standard electron-hole mapping, allowing us to describe a single electron vacancy in the valence band as a hole with positive charge and mass. We can thus understand the excitonic peak as a hydrogenoid bound state of an electron and a positively charged hole, indicated by the red dashed line enclosing the electron-hole pair. **c**, The intersubband absorbance of a doped QW containing only one localized state, and a continuum of states above the first ionization energy of the QW (E_i). Only the bound-to-continuum absorption is present, and no excitonic peak is visible³¹. As shown in the inset, in this case the continuum is due to each electron having multiple possible delocalized final states. **d**, The initially filled electron subband has a positive effective mass and the electron-hole mapping leads to a positively charged hole with negative effective mass, unable to form a bound state with the electron under the sole effect of the two-body Coulomb interaction.

To provide evidence of photon-mediated bound states, we realized a system similar to the one described in ref.⁴, composed of 13 GaAs/AlGaAs quantum wells embedded in highly confining, grating-shaped gold microcavity resonators. More details of the sample can be found in the Methods. The resonators are one-dimensional ribbons (or 1D patch cavities¹⁸), and the electromagnetic field (sketched in Fig. 2a) is almost completely confined below the metallic fingers. The sizes of the QWs were chosen to be thin enough to have a single trapped conduction subband, as the presence of a second subband would lead to the creation of intersubband polaritons¹⁹. Not only this would complicate the analysis of the data, but the presence of a bound-to-bound transition would almost saturate the available oscillator strength, leaving little for the bound-to-continuum transition we aim to measure. To check this important point, we fabricated two samples, HM4229 and HM4230, differing in QW width and doping. Sample HM4229 contains 4-nm-thick GaAs QWs (with width $L_{\text{QW}} = 4$ nm), each doped at a density $5 \times 10^{12} \text{ cm}^{-2}$, whereas sample HM4230 contains QWs with $L_{\text{QW}} = 3.5$ nm doped at $4.77 \times 10^{12} \text{ cm}^{-2}$.

As shown in Fig. 3b–e, bound-to-bound and bound-to-continuum transitions between different single-particle states of the QW potential undergo opposite frequency shifts when L_{QW} is reduced: the former are blueshifted, whereas the latter are redshifted. This allows us to assess the nature of the optical transition by looking at the transmission spectra of the two samples before gold deposition, shown in Fig. 3a.

Here we observe a very broad absorption that (being transverse magnetic polarized) stems from the doped QWs. We also observe a narrower feature around 140 meV that can be identified as the edge of the continuum. Crucially, this feature does not blueshift with decreasing L_{QW} . It shows a transfer of spectral weight towards the red part of the spectrum, whereas a bound-to-bound transition would have led to a blueshift of the order of tens of millielectronvolts, proving the bound-to-continuum nature of the transitions in the bare QWs.

Each sample was fabricated into metal–semiconductor–metal grating resonators with period D and metallic fingers of width p , as shown in Fig. 2a,b, and following a procedure similar to that used in ref.²⁰. As the electromagnetic field is extremely localized below the metallic fingers, the system essentially behaves as a Fabry–Perot cavity of length p (ref.¹⁸). More details can be found in the Methods.

We fabricated several grating-based devices, $200 \times 200 \mu\text{m}^2$ in area with p ranging from 800 nm to 5 μm , to span a vast range of frequencies with the resonant cavity modes (see Fig. 2b). Reflectance data were obtained for each device at a temperature of 78 K using a Fourier-transform infrared (FTIR) microscope equipped with a very compact cryostat. A schematic of the experimental set-up is shown in Fig. 2c. The main result of this work is reported in Fig. 4. In Fig. 4a, we plot the 78 K reflectivity map of the HM4229 sample as a function of the bare resonator frequency. Details of the spectroscopic characterization and the data analysis are provided in the Methods. Whereas above the ionization threshold (shown by a black

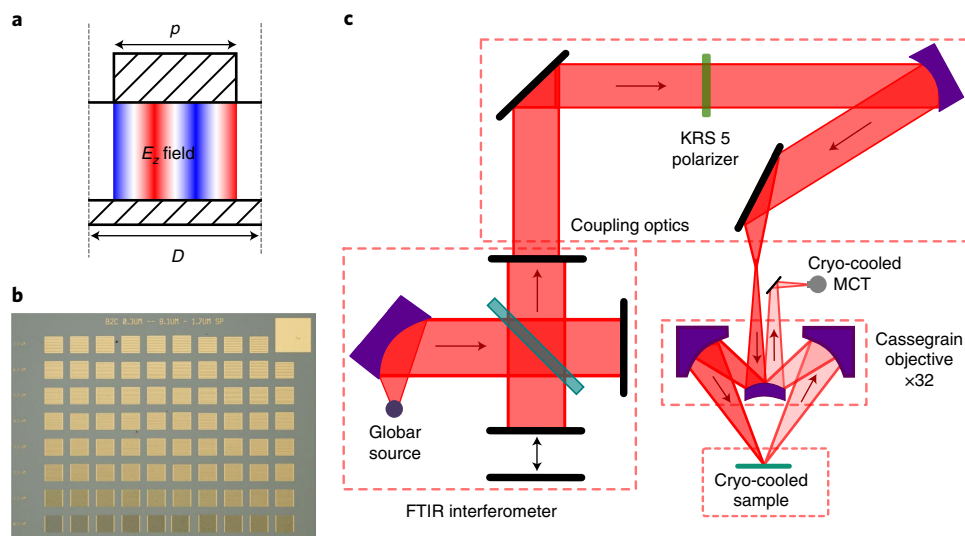


Fig. 2 | Schematics of the experimental set-up. **a**, Distribution of the electric field component orthogonal to the metallic layers for one period (D) of the structure and for the mode TM_{02} of the ribbon resonator. **b**, Optical microscope image of a typical sample set. Each device features a different finger width p . The top right device is a fully metallized surface that serves as mirror reference. **c**, The experimental set-up used for the reflectivity measurements. It consists of a mid-infrared microscope connected to an FTIR spectrometer. The source is a thermal globar lamp, and the detector is a liquid-nitrogen-cooled mercury-cadmium telluride (MCT). The incident beam is polarized normally to the metallic fingers using a KRS 5 (thallium bromo-iodide) mid-infrared polarizer, and the system operates in reflection. A compact, thin cryostat permits measurements to be performed down to a temperature of 78 K.

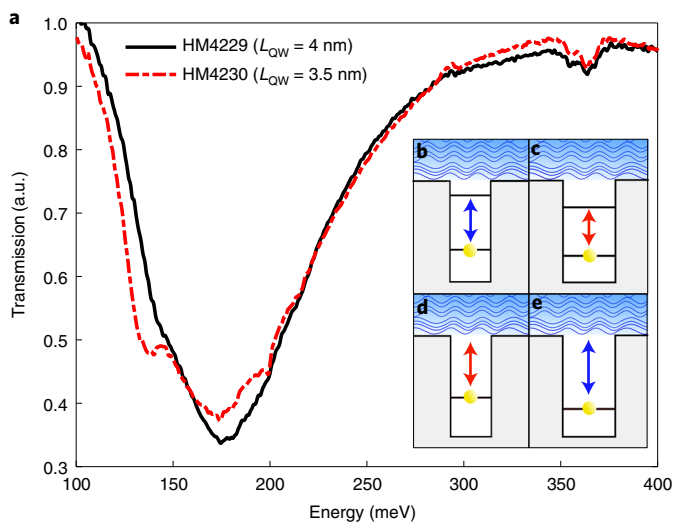


Fig. 3 | Bound-to-continuum nature of the optical transition in bare QWs with no surrounding photonic resonator. **a**, Transmission measured at 300 K for samples with QWs of different width L_{QW} . **b-e**, Schematic of bound-to-bound (**b,c**) and bound-to-continuum (**d,e**) transitions in doped QWs. The black horizontal lines indicate the single-particle bound states, whereas the wavy blue lines indicate the delocalized single-particle states above the ionization threshold. The QWs in **c** and **e** are thicker along the growth axis (larger L_{QW}). Blue and red double arrows highlight, respectively, the larger and the smaller transition energy for each kind of transition as the QW width is varied.

horizontal dashed line), we can observe an absorption continuum, below it a narrow polaritonic resonance appears. It is redshifted by more than 20 meV with respect to the bare resonator. Overlaid on the colour map we plot the peak frequencies obtained by a multiple Lorentzian fit of the data. Red triangles and blue squares are used respectively for frequencies below and above the identified

ionization threshold. For comparison, the green circles mark the frequency of the bare resonator, measured on an undoped sample (data in the Supplementary Information). In Fig. 4c, the respective linewidths are shown as a function of the resonant mode frequency.

Below the ionization threshold it appears that the lifetime of the discrete polaritonic mode is mainly limited by the resonator lifetime. Above it, we have a bound-to-continuum spectrum in which only very broadened and undefined features can be identified. To better illustrate this finding, in Fig. 4b we plot the reflectivity spectra of the doped sample (red curves) for different values of the bare resonator frequency, together with the resonator resonance measured on an undoped sample (green curves). From this, we can clearly observe how the doped sample develops a discrete resonance below the continuum edge, whereas an identical, but electromagnetically uncoupled, sample presents none.

Note that in Fig. 4a both the narrow discrete mode below the continuum edge (red) and the extracted peak of the broad continuum above it (blue) are at frequencies lower than the bare resonator (green). Moreover, they have very different linewidths that remain well separated for all cavity energies. These features are not compatible with a standard (bound-to-bound) polaritonic description, in which both the light and matter resonances are between the polaritonic modes due to mode repulsion. Moreover, in a simple Hopfield model²¹, the linewidths of the coupled modes are weighted averages of the uncoupled light and matter ones and they should thus cross over the polaritonic anticrossing. Data for sample HM4230 in the strong coupling regime are reported in the Supplementary Information. They are similar to the data presented here for HM4229 and point at the same conclusions.

Using the theory of ref. 4, such a hybrid discrete state can be described as a polariton whose electron density relative to the ground state one is given by

$$\Delta N(z) = P[|\psi^e(z)|^2 - |\psi^g(z)|^2], \quad (1)$$

where P , varying between 0 and 1, is the weight of the polaritonic matter component, $\psi^e(z)$ is the normalized wavefunction of an electron in its ground state, and $\psi^g(z)$ is the wavefunction of a localized

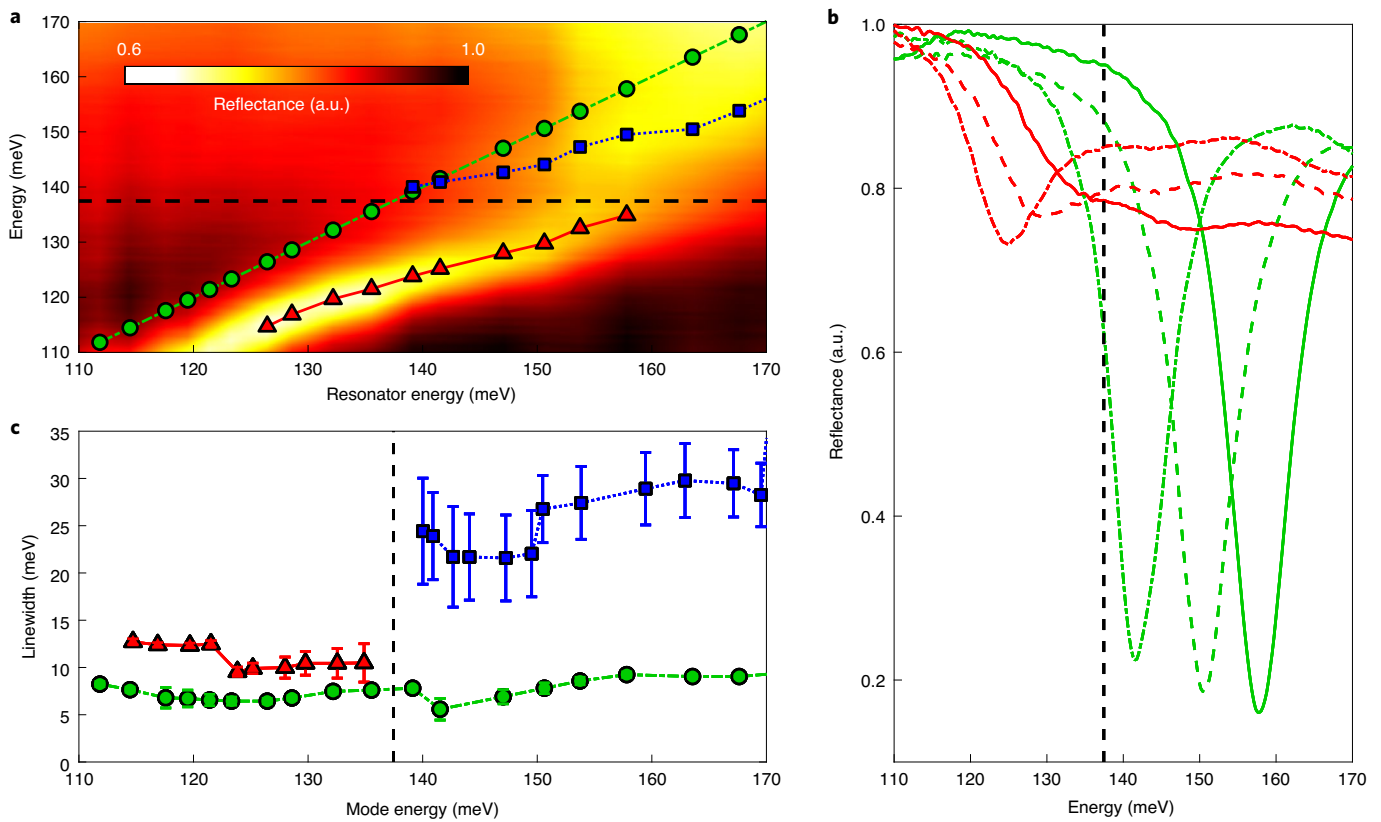


Fig. 4 | Experimental reflectivity data. **a**, Reflectance data from the doped sample HM4229 as a function of the resonator frequency. The peak positions extracted from the data are superimposed using blue squares and red triangles for the data points below and above the edge of the continuum, respectively. Green circles mark data from the undoped sample, taken as a reference for the cavity energy. **b**, Reflectance data for HM4229 (red) and the empty cavity (green) for resonator frequencies $\hbar\omega_c = 157.8$ meV (solid lines), $\hbar\omega_c = 147$ meV (dashed lines) and $\hbar\omega_c = 141.5$ meV (dot-dashed lines). **c**, Linewidths for the different modes as a function of the mode energy. Error bars are the 95% confidence intervals, determined via a multiple Lorentzian peak fitting procedure. In all panels the dashed black line marks the first ionization energy of the QW, labelled E_i in Fig. 1d.

electronic state generated by the light–matter interaction. In Fig. 5a, we use the model of ref. 4 to reproduce the observed reflectivity spectrum and compare it to the experimental data. Using the parameters of such a simulation we calculated P , which we plot in Fig. 5b. From this we can see that the discrete resonance below the ionization threshold is clearly defined for non-vanishing values of P , demonstrating a substantial occupation of the light-generated electronic wavefunction $\psi^e(z)$.

With this experiment, we demonstrated the possibility of strongly coupling a ionizing transition to a photonic resonator. As theoretically predicted, this results in a non-perturbative modification of the system's electronic structure. This leads to the appearance of a hybrid polaritonic excitation whose matter component is a bound state generated by the light–matter interaction, consisting of an electron and a hole kept together by their interaction with the transverse electromagnetic field. The experiment reported in this work measures only the optical properties of the system. However, an immediate question arises: can these bound states conduct electrical currents? If so, this would imply that they can act as discrete and tunable current channels into bright states, and it has been predicted that they could thus allow dramatic increases in the efficiency of intersubband mid-infrared emitters²². Initial work in this direction, albeit for a bound-to-bound transition, has been recently reported in mid-infrared detectors operating in the strong light–matter coupling regime²³.

The possibility of tuning material properties through coupling to a microcavity photonic field has been much discussed recently,

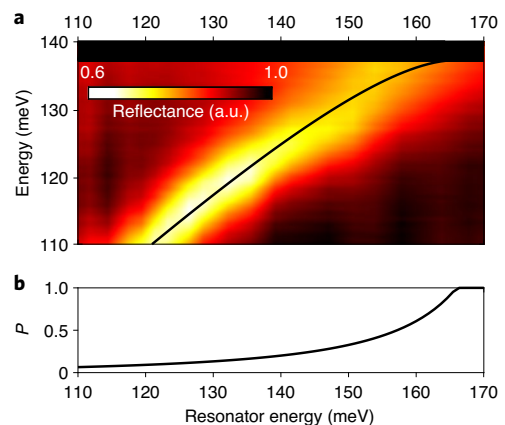


Fig. 5 | Calculation of P . **a**, The eigenmodes obtained by our theoretical model with parameters chosen to fit the experimental reflectance data in the colour map. Above the ionization threshold, it is uniformly black as the discrete modes used in the numerical diagonalization are too closely spaced to be resolved. **b**, The parameters extracted from **a** are used to calculate P for the discrete polariton mode.

with particular attention on chemical and structural properties^{24–26}. Beyond the boundary of mid-infrared optoelectronics, our results demonstrate that cavity quantum electrodynamics can be used as

tool in quantum material engineering, not only for shifting and hybridizing resonances, but non-perturbatively and controllably changing their nature.

Finally, one tantalizing feature of the discrete resonances we observe is their conceptual proximity with Cooper pairs, bound states of two electrons bound by the exchange of virtual phonons¹⁷. Theoretical proposals suggest that the critical temperature of a superconductor could be modified by coupling electrons through the exchange of virtual polaritons^{25,28,29} or virtual cavity photons²⁵, and a first experimental result was very recently reported³⁰. The excitations we observed here differ in multiple fundamental aspects from Cooper pairs, including the fact they are electrically neutral and have a finite lifetime due to their polaritonic nature. Still, they demonstrate that it is possible to bind two particles not via Coulomb interactions but through the exchange of photonic excitations mediated by a judiciously engineered resonator.

Online content

Any methods, additional references, Nature Research reporting summaries, source data, extended data, supplementary information, acknowledgements, peer review information; details of author contributions and competing interests; and statements of data and code availability are available at <https://doi.org/10.1038/s41567-020-0994-6>.

Received: 26 January 2020; Accepted: 3 July 2020;

Published online: 17 August 2020

References

- Nikonov, D. E., Imamoğlu, A., Butov, L. V. & Schmidt, H. Collective intersubband excitations in quantum wells: Coulomb interaction versus subband dispersion. *Phys. Rev. Lett.* **79**, 4633–4636 (1997).
- Frisk Kockum, A., Miranowicz, A., De Liberato, S., Savasta, S. & Nori, F. Ultrastrong coupling between light and matter. *Nat. Rev. Phys.* **1**, 19–40 (2019).
- Forn-Díaz, P., Lamata, L., Rico, E., Kono, J. & Solano, E. Ultrastrong coupling regimes of light-matter interaction. *Rev. Mod. Phys.* **91**, 025005 (2019).
- Cortese, E., Carusotto, I., Colombelli, R. & De Liberato, S. Strong coupling of ionizing transitions. *Optica* **6**, 354–361 (2019).
- Ballarini, D. & De Liberato, S. Polaritonics: from microcavities to sub-wavelength confinement. *Nanophotonics* **8**, 641–654 (2019).
- Khurgin, J. Excitonic radius in the cavity polariton in the regime of very strong coupling. *Solid State Commun.* **117**, 307–310 (2001).
- Citrin, D. S. & Khurgin, J. B. Microcavity effect on the electron-hole relative motion in semiconductor quantum wells. *Phys. Rev. B* **68**, 205325 (2003).
- Khurgin, J. B. Pliable polaritons: Wannier exciton-plasmon coupling in metal-semiconductor structures. *Nanophotonics* **8**, 629–639 (2018).
- Yang, M.-J., Kim, N. Y., Yamamoto, Y. & Na, N. Verification of very strong coupling in a semiconductor optical microcavity. *N. J. Phys.* **17**, 023064 (2015).
- Brodbeck, S. et al. Experimental verification of the very strong coupling regime in a GaAs quantum well microcavity. *Phys. Rev. Lett.* **119**, 027401 (2017).
- Anappara, A. A. et al. Signatures of the ultrastrong light-matter coupling regime. *Phys. Rev. B* **79**, 201303 (2009).
- Todorov, Y. et al. Ultrastrong light-matter coupling regime with polariton dots. *Phys. Rev. Lett.* **105**, 196402 (2010).
- Günter, G. et al. Sub-cycle switch-on of ultrastrong light-matter interaction. *Nature* **458**, 178–181 (2009).
- Levinsen, J., Li, G. & Parish, M. M. Microscopic description of exciton-polaritons in microcavities. *Phys. Rev. Res.* **1**, 033120 (2019).
- Averkiev, N. S. & Glazov, M. M. Light-matter interaction in doped microcavities. *Phys. Rev. B* **76**, 045320 (2007).
- Haken, H. *Quantum Field Theory of Solids: An Introduction* (North-Holland, 1976).
- Cooper, L. N. Bound electron pairs in a degenerate fermi gas. *Phys. Rev.* **104**, 1189–1190 (1956).
- Todorov, Y. et al. Optical properties of metal-dielectric-metal microcavities in the thz frequency range. *Opt. Express* **18**, 13886–13907 (2010).
- Dini, D., Köhler, R., Tredicucci, A., Biasiol, G. & Sorba, L. Microcavity polariton splitting of intersubband transitions. *Phys. Rev. Lett.* **90**, 116401 (2003).
- Manceau, J.-M. et al. Resonant intersubband polariton-phonon scattering in an optically pumped polaritonic device. *Appl. Phys. Lett.* **112**, 191106 (2018).
- Hopfield, J. Theory of the contribution of excitons to the complex dielectric constant of crystals. *Phys. Rev.* **112**, 1555–1567 (1958).
- De Liberato, S. & Ciuti, C. Quantum theory of electron tunneling into intersubband cavity polariton states. *Phys. Rev. B* **79**, 075317 (2009).
- Vigneron, P.-B. et al. Quantum well infrared photo-detectors operating in the strong light-matter coupling regime. *Appl. Phys. Lett.* **114**, 131104 (2019).
- Galego, J., Garcia-Vidal, F. J. & Feist, J. Cavity-induced modifications of molecular structure in the strong-coupling regime. *Phys. Rev. X* **5**, 041022 (2015).
- Ebbesen, T. W. Hybrid light-matter states in a molecular and material science perspective. *Acc. Chem. Res.* **49**, 2403–2412 (2016).
- Ruggenthaler, M., Tancogne-Dejean, N., Flick, J., Appel, H. & Rubio, A. From a quantum-electrodynamical light-matter description to novel spectroscopies. *Nat. Rev. Chem.* **2**, 1–16 (2018).
- Laussy, F. P., Kavokin, A. V. & Shelykh, I. A. Exciton-polariton mediated superconductivity. *Phys. Rev. Lett.* **104**, 106402 (2010).
- Schlawin, F., Cavalleri, A. & Jaksch, D. Cavity-mediated electron-photon superconductivity. *Phys. Rev. Lett.* **122**, 133602 (2019).
- Curtis, J. B., Raines, Z. M., Allocca, A. A., Hafezi, M. & Galitski, V. M. Cavity quantum eliasberg enhancement of superconductivity. *Phys. Rev. Lett.* **122**, 167002 (2019).
- Thomas, A. et al. Exploring superconductivity under strong coupling with the vacuum electromagnetic field. Preprint at <http://arXiv.org/abs/1911.01459v1> (2019).
- Capasso, F. et al. Observation of an electronic bound state above a potential well. *Nature* **358**, 565–567 (1992).

Publisher's note Springer Nature remains neutral with regard to jurisdictional claims in published maps and institutional affiliations.

© The Author(s), under exclusive licence to Springer Nature Limited 2020

Methods

Sample growth and fabrication. The samples were grown by molecular beam epitaxy on semi-insulating 2" GaAs wafers. The process starts with a 500-nm-thick $\text{Al}_{0.50}\text{Ga}_{0.50}\text{As}$ stop layer, followed by the deposition of 13 layers of GaAs QWs in $\text{Al}_{0.33}\text{Ga}_{0.67}\text{As}$ barriers; it ends with a 30-nm-thick GaAs cap layer. The two samples differ in terms of L_{QW} and introduced electronic doping, whereas the barriers are always 10 nm thick. Sample HM4229 contains GaAs QWs with $L_{\text{QW}} = 4$ nm, whereas sample HM4230 contains QWs with $L_{\text{QW}} = 3.5$ nm. Si doping is introduced in the centre of the AlGaAs barriers as δ -doping, yielding 2D electron densities in the wells (measured at 300 K) of $5 \times 10^{13} \text{ cm}^{-2}$ (HM4229) and $4.77 \times 10^{13} \text{ cm}^{-2}$ (HM4230), respectively.

The metal–semiconductor–metal resonators were realized by bonding the samples with gold–gold thermocompression onto undoped GaAs wafers, following the procedure used in ref. ²⁰. After substrate removal, the resonators were defined with e-beam lithography followed by metal evaporation (Ti/Au) and lift-off.

Ribbon resonators. The use of metal–semiconductor–metal resonators is important, as it permits coupling to intersubband transitions that are TM polarized, even at normal incidence. In this case, however, the extreme thinness of the active region (~ 260 nm) prevents operation in the photonic crystal regime³², and places the system in the independent resonator regime instead. The resonance frequency f of the Fabry–Perot resonator is set by p , and not by D , according to the simple formula

$$\frac{c}{f} = \frac{2n_{\text{eff}}p}{m}, \quad m \in \mathbb{N}, \quad (2)$$

where c is the speed of light and n_{eff} is an effective index that takes into account the reflectivity phase at the metallic boundaries.

We decided to use the cavity mode with $m = 2$, instead of the fundamental mode with $m = 0$ that is typically used in these systems, to simplify the fabrication procedure and increase the electromagnetic overlap factor. This is evident from Fig. 2a, which highlights three nodal lines for the resonant cavity mode.

Spectroscopic characterization. The transmission spectra of the samples before wafer bonding were acquired with standard multipass waveguide transmission measurements after the samples were metallized with Ti/Au on the top surface and 45° facets were shaped with mechanical polishing. The measurements were performed with an FTIR spectrometer, equipped with a thermal globar source, and a deuterated triglycine sulfate detector.

The reflectivity measurements were performed with a microscope connected to the FTIR spectrometer. The microscope optics/mirrors operated in the mid-IR, the source was a thermal globar and the detector was a liquid-nitrogen-cooled mercury–cadmium telluride. Light was focused on the sample with a Cassegrain objective that operates at a fixed incidence angle of incidence of $20^\circ \pm 5^\circ$. A very thin cryostat (Linkam LNP96) fits below the microscope objectives and permits the reflectivity measurements to be performed at a temperature of 78 K.

Fitting procedure. Both the resonances and the lifetimes shown in Fig. 4 were obtained from the experimental reflectance dataset for each metal stripe size, through an automatic multiple Lorentzian peak fitting procedure. The same fitting model was used for the data of both doped and undoped samples.

To calculate the matter component P , we used the same procedure developed in ref. ⁴, where the doping and the ionization energy are adjustable parameters.

Data availability

The data that support the findings of this study are available from the corresponding authors on reasonable request. Source data are provided with this paper.

Code availability

The codes that support the findings of this study are available from the corresponding author (S.D.L.) on reasonable request.

References

32. Chassagneux, Y. et al. Electrically pumped photonic-crystal terahertz lasers controlled by boundary conditions. *Nature* **457**, 174–178 (2009).

Acknowledgements

S.D.L. is a Royal Society Research Fellow and was partly funded by the Philip Leverhulme Prize of the Leverhulme Trust. R.C., J.M.-M., G.B. and I.C. were partly funded by the European Union FET-Open Grant Number MIR-BOSE 737017. R.C. and A.B. were partly funded by the French National Research Agency (project IRENA). This work was partly supported by the French RENATECH network.

Author contributions

S.D.L. supervised the project and led the theoretical work. I.C., R.C. and S.D.L. designed the experiment. R.C. led the experimental work. G.B. grew the sample and N.-L.T. fabricated the devices. N.-L.T., J.-M.M. and A.B. carried out the optical characterization. E.C. performed the data analysis. All authors discussed the data and contributed to the manuscript.

Competing interests

The authors declare no competing interests.

Additional information

Supplementary information is available for this paper at <https://doi.org/10.1038/s41567-020-0994-6>.

Correspondence and requests for materials should be addressed to R.C. or S.D.L.

Reprints and permissions information is available at www.nature.com/reprints.